Influence of Deep-Ocean Warming on Coastal Sea-Level Trends in the Gulf of Mexico

Jacob M. Steinberg[1], Christopher G. Piecuch[1], Benjamin D. Hamlington[2], Phillip R. Thompson[3], Sloan Coats[3]

[1]Physical Oceanography Department, Woods Hole Oceanographic Institution, Woods Hole, MA USA
[2]Jet Propulsion Laboratory, Pasadena, CA, USA
[3]University of Hawaii at Mānoa, Honolulu, HI, USA

Key Points:

- Recently observed sea-level trends along the US Gulf coast are consistent with higher future sea-level rise scenarios.
- Subsurface ocean warming has caused mass redistribution within the Gulf of Mexico contributing to positive coastal sea-level trends.
- Mass redistribution within and mass import into the Gulf of Mexico explain a dominant fraction of eastern Gulf trends in sea-level.

Corresponding author: Jacob M. Steinberg, jsteinberg@whoi.edu

Abstract

Rates of sea-level rise are increasing across the global ocean. Since $\sim$ 2008, sea-level acceleration is particularly pronounced along the US Gulf of Mexico coastline. Here we use model solutions and observational data to identify the physical mechanisms responsible for enhanced rates of recent coastal sea-level rise in this region. Specifically, we quantify the effect of offshore subsurface ocean warming on coastal sea-level rise and its relationship to regional hypsometry. Using the Estimating the Circulation and Climate of the Ocean (ECCO) Version 5 ocean state estimate, we establish that coastal sea-level changes are largely the result of changes in regional ocean mass, reflected in ocean bottom pressure, on interannual to decadal timescales. These coastal ocean bottom pressure changes reflect both net mass flux into and out of the Gulf, as well as internal mass redistribution within the Gulf, which can be understood as an isostatic ocean response to subsurface offshore warming. We test the relationships among coastal sea-level, ocean bottom pressure, and subsurface ocean warming predicted by the model using data from satellite gravimetry, satellite altimetery, tide gauges, and Argo floats. Our estimates of mass redistribution explain a significant fraction of coastal sea-level trends observed by tide gauges. For instance, at St. Petersburg, Florida, this mass redistribution accounts for $> 50\%$ of the coastal sea-level trend observed over the 2008-2017 decade. This study elucidates a physical mechanism whereby coastal sea-level responds to open-ocean subsurface warming and motivates future studies of this linkage in other regions.

Plain Language Summary

We investigate drivers of coastal sea-level rise in the Gulf of Mexico. Using both model output and observational data we consider the relationship between warming of the ocean at depths below the surface and away from the coast and sea-level rise at the coast. Imprints of this relationship are identified in an observational dataset of pressure at the seafloor. Changes in these pressures throughout the Gulf of Mexico over decadal periods reveal a redistribution of water from deeper to shallower regions that coincides with warming throughout the water column. This analysis incorporates observations of coastal sea-level from tide gauges along the US Gulf of Mexico coast, ocean temperature and salinity from profiling floats, ocean bottom pressures from satellite gravimetry, and sea surface height from satellite altimetry. Results reveal that offshore warming below the surface contributes importantly to coastal sea-level rise. Its relative contribution is greater in the eastern Gulf, where rates of vertical land motion are smaller than in the western Gulf.

1 Introduction

Understanding the causes and drivers of regional sea-level variability is important for the global population living at the coast. With this understanding, communities can strategically plan to respond to current and future impacts within the context of regional climatic and geologic forcings. Tide gauge records are some of the longest instrumental measurements of relative sea-level (RSL) that enable observed variability to be linked to physical processes with daily to centennial timescales. Of the physical processes responsible for coastal RSL trends (e.g., glacial isostatic adjustment, naturally or anthropogenically driven vertical land motion (VLM), terrestrial water storage loss, steric expansion, changing ocean dynamics), impacts of both local and remote ocean warming remain under explored. This is partly due to the need, in addition to long-term tide gauge records, for observations of the various processes contributing to coastal sea-level changes (Woodworth et al., 2019). In this work, we take a mechanistic approach to better understand how open-ocean warming contributes to coastal RSL rise on decadal timescales.

The Gulf of Mexico (GOM) is a marginal sea that, over the recent decades, has experienced rates of sea-level rise greater than the global mean (Sweet et al. (2022), Fig.

2.1) (Fig. 1). Recent analyses of past and extrapolations for future sea-level along the US coast (Sweet et al., 2022; Hamlington et al., 2022) identify the eastern GOM as unique in that observations-based extrapolations through 2050 align with the highest of five model-based future sea-level rise scenarios (Sweet et al., 2017). Additionally, unlike in other regions considered in the report, model-based sea-level timeseries in the eastern GOM disagree with current observations, and scenarios and extrapolations diverge to a greater degree by 2050. These differences provide motivation to explore why the GOM is unique and consider regionally relevant physical processes within the GOM that may be responsible for driving an increase in RSL rise and divergence from predictions.

Previous efforts to explain coastal RSL rise in the GOM and along the US east coast reveal impacts of VLM on tide gauge records, effects of shifting atmospheric patterns, and connections to larger-scale ocean warming over the subtropical North Atlantic ocean (Kolker et al., 2011; Thompson & Mitchum, 2014; Volkov et al., 2019; Liu et al., 2020). These analyses highlight the spatial co-variance of coastal sea-level variations south of Cape Hatteras and reveal that land subsidence plays a large role in RSL rise in the western GOM. They also connect warming driven sea-level rise throughout the GOM to heat divergence in the North Atlantic subtropical gyre. These results inform interpretations of spatio-temporal patterns apparent in tide gauge records, but they do not amount to comprehensive attributions of the observed changes, and are only parts of a story in which GOM sea-level and its variability relate to physical processes within the GOM.

We consider ocean mass and heat content changes in the GOM and reveal a physical mechanism that can explain a significant fraction of RSL rise experienced at the coast. We consider relationships among changes in ocean density, ocean bottom pressure, and bathymetry as they shape the expression of open-ocean variability at the coast (Vinogradova et al., 2007; Bingham & Hughes, 2012). These relationships reveal the effect of ocean warming on coastal sea-level as a function of the depth at which warming occurs and motivate consideration of hypsometry, the distribution of ocean area with depth, in generalizing these results. By characterizing subsurface warming in this way, we explain interannual trends in coastal sea-level identifying an underlying physical mechanism that can be used to anticipate future behavior based on patterns of warming. Specifically, we focus on sea-level trends at the 10-year timescale, hereafter referred to as decadal. This choice was made to investigate relationships between ocean warming and coastal sea-level at sub-seasonal frequencies such that observed variability can be explained in the context of climate scale changes.

In this investigation we use both model solutions and measurements made by a diverse set of observational platforms to identify a mechanism relating subsurface ocean warming to coastal RSL rise. Throughout the GOM, and in the eastern GOM in particular, this mechanism is responsible for a significant fraction of sea-level rise observed at the coast. That this relationship is apparent in both models and observations of the past few decades motivates future work to determine the effects of varied bathymetry and patterns of earlier and future warming on coastal sea-level. The remainder of this paper is structured as follows: Section 2 describes the model, the spatial dependence on the correlation between ocean bottom pressure and sea surface height, the framework employed to describe warming-driven mass redistribution, and the sensitivity to the time period of consideration. Section 3 details the application of this warming-driven mass redistribution framework to observations spanning the 2010-2020 period, during which decadal sea-level trends in the eastern GOM are at a near maximum. Section 4 offers discussion, conclusions, and future directions.

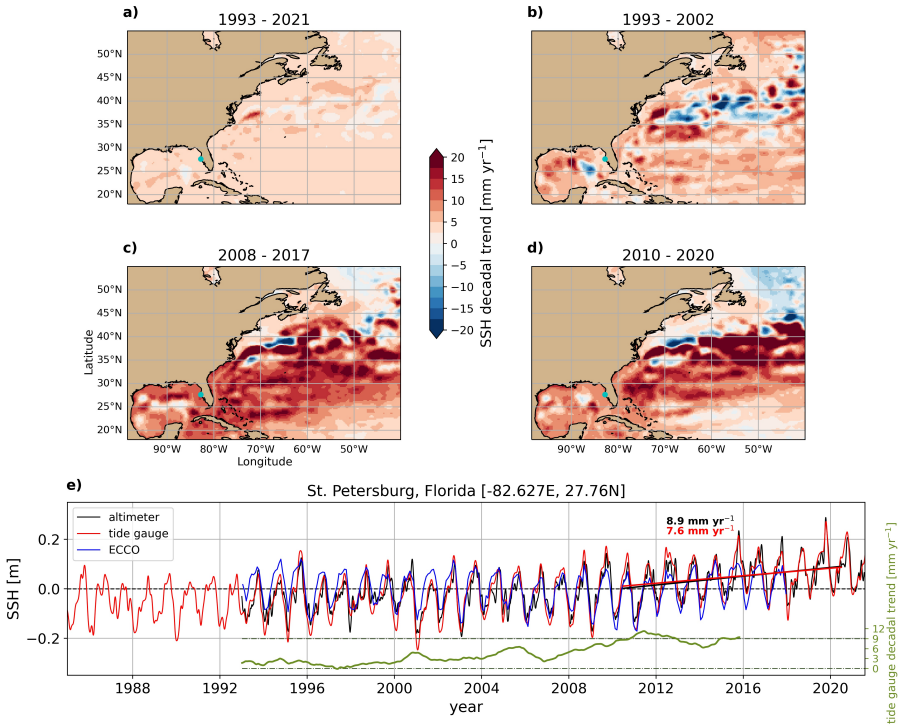

Figure 1. a) 1993-2021 linear SSH trends [mm yr^{-1}] in the GOM and North Atlantic. b) Sames as (a), but for 1993-2002 c) 2008-2017 d) 2010-2020 e) Timeseries of SSH at the St. Petersburg, Florida tide gauge station referenced to the 1993-2021 mean. Daily tide gauge measurements smoothed with a 30-day boxcar filter are in red, gridded altimeter SSH closest to the tide gauge location and temporally smoothed with a 30-day boxcar filter are in black, and ECCO monthly SSH from the grid cell closest to the tide gauge location are in blue. Altimeter measurements and ECCO ouput begin in 1993. A linear trend is fit to tide gauge and altimeter measurements over the 2010-2020 period. A moving decadal trend, beginning in 1988, calculated from the tide gauge record after removal of a seasonal cycle, is in green. Trends are centered on the midpoint month of each decade.

2 ECCO

2.1 State Estimate

The ECCO Version 5 state estimate applies a nonlinear inverse modeling framework to constrain a Boussinesq general circulation model run on the latitude-longitude-cap (LLC) 270 grid to in-situ and remotely sensed observations (Wunsch & Heimbach, 2007; Wunsch et al., 2009; Forget et al., 2015). This model is freely running and physically consistent. Atmospheric reanalysis products are used in bulk formulae for heat and freshwater forcing while wind-stress forcing is prescibed directly. The LLC270 grid has a nominal horizontal resolution of 1/3°, varying between 12 and 28 km, and with 50 vertical levels. Vertical resolution is 10 m in the near surface layers decreasing to $\sim$ 400 m in the deepest layer. As we are interested change on decadal time scales, monthly output over the full 25-year period (1993-2017) are obtained from the ECCO Consortium database [www.ecco-group.org]. Within the GOM, depths do not exceed $\sim$ 3500 m and are less than $\sim$ 1000 m over nearly 50% of the basin (Fig. 2). For subsequent calculations, a mask is defined for the GOM, with boundaries spanning the Florida-Cuba and Cuba-Yucatan gaps (Fig. 2a, red line).

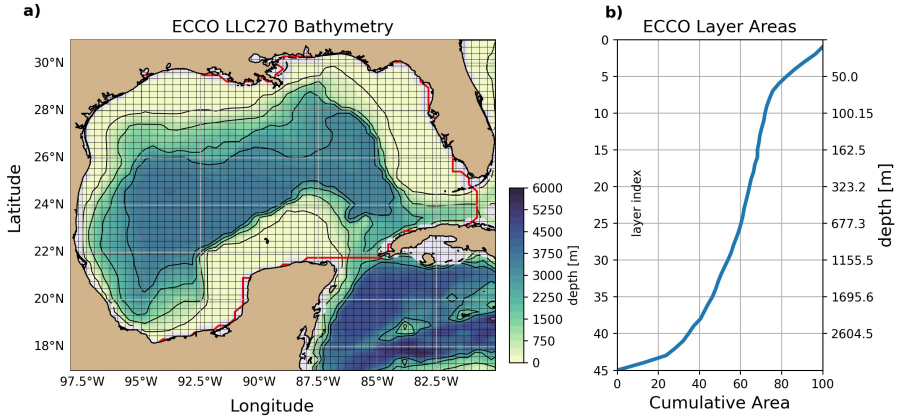

Figure 2. a) ECCO GOM bathymetry with LLC270 grid lines. Red line identifies the eastern and southern edges of the mask used to define the GOM surface area. b) Cumulative area of ECCO vertical layers summing from the deepest layer in the Gulf to the surface.

Past studies show various aspects of ECCO state estimate realism, particularly the model's ability to reproduce observed patterns in SSH, sea surface temperature, and ocean heat content at regional and large scales (e.g., Buckley and Marshall (2016); Thompson et al. (2016); Piecuch et al. (2017, 2019); Fukumori et al. (2018)). Comparison to satellite-altimeter measurements of SSH variability throughout the GOM and sea-level observations at the St. Petersburg, Florida tide-gauge station shows good model-observation correspondence (Figs. 1e, 3a,b). This comparison highlights ECCO's ability to reproduce a seasonal cycle as well as interannual variability and trends like those observed in both tide gauge and altimeter measurements, specifically over the 2008-2017 decade where basin-mean trends in observations and ECCO both excede 5 mm yr^{-1} (9.5 and 6.8, respectively). While the ECCO and observations-based timeseries (Fig. 1e) do not represent independent comparisons, they demonstrate the model's consistency with the data. The lack of mesoscale features apparent in Figure 3a and absent in Figure 3b, is the result of downweighting of altimeter observations in a state estimate designed to reproduce regional and large scale patterns and limited in horizontal resolution. For these reasons, ECCO derived trends are generally smaller in magnitude than observation-based trends. These results provide confidence that ECCO is an informative tool to use in exploring large-scale decadal sea-level trends in the GOM.

2.2 SSH, Bottom Pressure, and Steric Height

Following Gill and Niler (1973), changes in sea-level ζ can be written as the sum of ocean bottom pressure ζ_b and steric ζ_ρ contributions,

$$\zeta = \zeta_b + \zeta_\rho = \frac{p_b}{\rho_0 g} + \frac{-1}{\rho_0}\int_{-H}^{0}(\rho - \rho_0)dz, \tag{1}$$

where p_b is bottom pressure, ζ_b is the equivalent expressed in SSH units, $\rho_0 = 1029$ kg m^{-3}, g is gravitational acceleration, and H is seafloor depth. In this construction, ζ and p_b represent deviations from a time mean. In-situ density ρ is calculated following Jackett and McDougall (1995) (using the Python script jmd95.py, https://mitgcm.readthedocs.io) from ECCO temperature and salinity fields. The relative extent to which sea-level variability reflects bottom pressure and steric changes depends on ocean depth, latitude, stratification, horizontal scale, and timescale. Comparison of timeseries in the GOM reveals consistency with the expectation that away from the coast over the deep ocean, ζ changes

correspond to ζ_ρ changes, while over shallow depths near the coast, changes in ζ match ζ_b (Vinogradova et al., 2007). The fraction of monthly ζ variance explained by bottom pressure changes, defined as $1 - \langle \zeta - \zeta_b \rangle / \langle \zeta \rangle$ where $\langle\rangle$ denotes a temporal variance, is greater than 0.5 shore-ward of the $\sim$ 100 m isobath (Fig. 3b, yellow contour). This dependence on depth is apparent in Eq. 1 where ζ becomes ζ_b in the limit that H goes to zero (Bingham & Hughes, 2012).

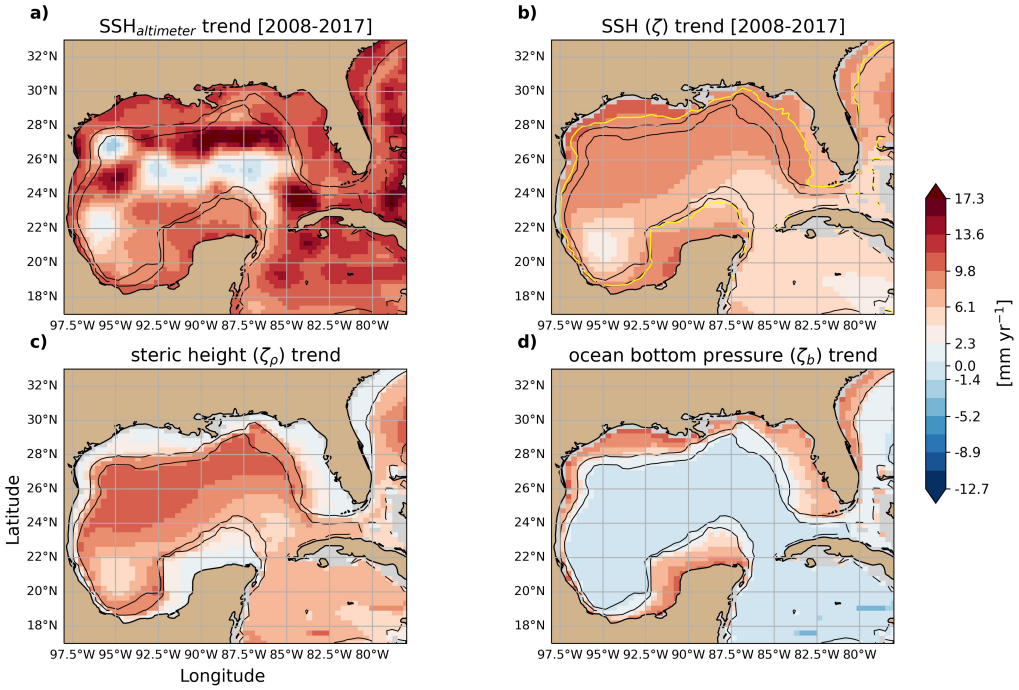

Figure 3. a) Linear trend fit over the 2008-2017 decade in altimeter derived SSH. Here, daily timeseries are first smoothed with a 30-day boxcar filter. Black contours identify the 150 m and 1000m isobaths. b) Linear trend (2008-2017 decade) in ECCO SSH. The yellow contour corresponds to the 0.5 fraction of ζ variance explained by ζ_b. c) Linear trend (2008-2017 decade) in ECCO steric height ζ_ρ and d) ECCO manometric sea-level ζ_b. The diverging colormap is aligned such that the midpoint color (white) corresponds to the GOM area-mean ζ_b trend ($\overline{\zeta_b}$).

In the GOM, relative contributions to ζ trends from ζ_ρ and ζ_b generally align with bathymetric contours (Fig. 3b-d). While these relationships depend on time scale, this characterization is relevant as we are interested in decadal trends. In an additive sense these decadal trends in ζ_ρ and ζ_b together reproduce a ζ trend map with significantly less spatial structure than the contributing parts. In other words, sea-level rise at decadal timescales in the GOM is relatively spatially homogeneous compared to patterns of steric and mass changes. This homogeneity is less apparent in altimeter derived trend maps (Fig. 3a) where eddies with sub-decadal timescales add smaller-scale spatial structure. That the basin mean trend in ζ_b is positive indicates an increase in mass to the GOM at a rate of $\sim$ 2.3 mm yr^{-1} (Fig. 3d). This trend is similar to the barystatic sea-level trend over the same period (Gregory et al., 2019) and is set as the midpoint value of the colorbar in Figure 3. The spatial variability in ζ_b trends identifies mass redistribution within the GOM, namely a transfer from the deeper parts of the basin (H $\gtrsim$ 150 m) to-

wards the coast. In the next section we develop an analytic model to relate the spatial structure in Figure 3d to subsurface warming.

2.3 Analytic Model

To elucidate the spatial pattern of decadal trends in ζ_b, which control ζ changes at the coast (Fig. 3), we consider a condition of no motion with no horizontal gradients in SSH (c.f. 3b),

$$\nabla\zeta = 0, \tag{2}$$

where $\nabla = \partial/\partial x, \partial/\partial y$. Here we suppress trend notation for simplicity, but note that the derivation that follows has decadal trends in mind. This implies that SSH at any location is equal to the spatial average as

$$\zeta = \overline{\zeta}. \tag{3}$$

Writing both the local and spatial mean ζ as a sum of steric and bottom pressure terms, Equation 3 becomes

$$\zeta_\rho + \zeta_b = \overline{\zeta_\rho} + \overline{\zeta_b}. \tag{4}$$

Subtracting $\overline{\zeta_b}$ from both sides and rearranging, we find that any difference in local manometric sea level from its spatial mean can be expressed as the result of local steric changes,

$$\zeta_b' = -(\zeta_\rho - \overline{\zeta_\rho}), \tag{5}$$

where $\zeta_b' = \zeta_b - \overline{\zeta_b}$. The ζ_b' response described by Equation 5 is analagous to the well-known inverted barometer effect as discussed by Greatbatch (1994) but with "forcing" by ζ_ρ rather than barometric pressure. Greatbatch (1994) and Ponte (2006) discuss how this the static equilibrium solution is much greater in magnitude than the corresponding dynamic adjustment response.

To consider density driven changes in ζ_b in a model with discrete levels, we next write ζ_ρ as

$$\zeta_\rho = -\frac{1}{\rho_0}\sum_{i=1}^{N}(\rho_i - \rho_0)h_i, \tag{6}$$

a sum across N vertical layers where h_i denotes layer i thickness and ρ_i is the mean layer density. This expression considers the special case of density changes only as a function of depth. The area-weighted average is then

$$\overline{\zeta_\rho} = -\frac{1}{\rho_0}\sum_{i=1}^{N}\frac{A_i}{A_s}(\rho_i - \rho_0)h_i \tag{7}$$

where A_i is the area of layer i and A_s the total surface area. Inserting Eq. 6 and Eq. 7 into Eq. 5, we find

$$\zeta_{bi}^* = \frac{1}{\rho_0}\sum_{i=1}^{i}\left(1 - \frac{A_i}{A_s}\right)(\rho_i - \rho_0)h_i - \frac{1}{\rho_0}\sum_{i+1}^{N}\frac{A_i}{A_s}(\rho_i - \rho_0)h_i \tag{8}$$

where $\zeta_{bi}^* = \frac{p_{bi}}{g\rho_0}$ is the density driven manometric sea-level change at each layer i depth. This expression is identical to that presented in Landerer et al. (2007), where changes

in bottom pressure are now demonstrated as a steric response to ocean warming. Density changes drive a change in ζ_b that is only a function of depth, defined at each layer index i. This can be understood as the difference between area weighted steric contributions above and below each layer midpoint depth. This predicted quantity is hereafter referred to as ζ_b^*.

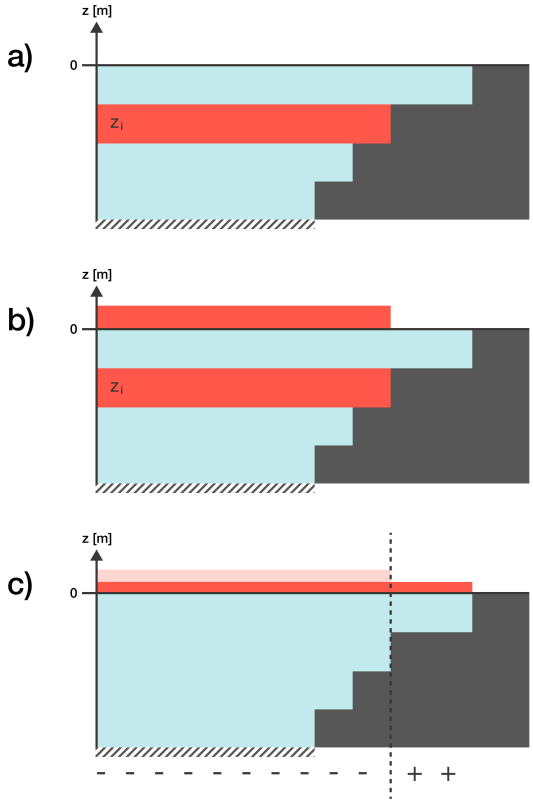

Figure 4. Redistribution schematic sequence, similar to Landerer et al. (2007), for an idealized four layer ocean with simple bathymetry (grey). a) Warming initially imagined in layer z_i. b) Warming coincides with a positive steric height response in SSH (red band above z=0) over the area extent of layer z_i. c) Equilibrium SSH after adjustment. The lightly shaded region is the initial change in SSH in b. Pluses and minuses below the sea floor show the corresponding changes in ocean bottom pressure.

The model derived above can be understood to anticipate a redistribution of mass, driving changes in ζ_b, following warming in some subsurface layer of the ocean. The sequence of events that result in these changes in ζ_b are shown schematically in Figure 4, where warming of some middle layer in a discretely layered ocean results in a positive change in ζ_b at depths shallower than the depth of warming. This change, positive in shallow regions and negative in regions with depths equal to or greater than the depth of warming, is the result of movement of water driven by a horizontal pressure gradient (Fig. 4b). As discussed in Greatbatch (1994), the static equilibrium solution of interest dominates a dynamic equilibrium solution and follows the rapid transient adjustment process. This mechanistic framework can be tested in ECCO on decadal timescales by comparing trends in ζ_b and ζ_b^*.

2.4 Results

We first consider the 2008-2017 decade as it is the most recent decade of model output and coincides with the increase in observed rates of sea-level rise throughout the GOM. Using GOM average layer densities, ζ_b^* is calculated and referenced to the ten year time-mean vertical profile. Model ζ_b values are averaged across all GOM grid points within each layer depth range, the GOM basin-mean timeseries is removed, and the result similarly defined relative to a ten year time-mean profile. Comparison of ζ_b^* and ζ_b' timeseries reveals qualitative similarity with variability dominated by a seasonal cycle and less pronounced trend (Fig. 5a,b). Quantitatively, the fraction of ζ_b' variance explained by ζ_b^* is $\gtrsim 75\%$ at nearly all depths. Where it dips below 75%, ζ_b' values are near zero. To characterize temporal variability at each depth and determine the linear trend over the 2008-2017 period, a simultaneous seasonal cycle plus linear trend is fit at each depth[1]. The fraction of ζ_b' variance explained by this fit to ζ_b^* is a slight increase over ζ_b^* itself as a result of removing nonseasonal variability.

Direct comparison of ζ_b^* and ζ_b' decadal trends against depth reveal marked agreement (Fig. 6). Trends are positive on the shelf, greatest at the coast decreasing to zero at ~ 150 m, and negative along the slope and in deeper regions. The spread in ζ_b' trends at each depth reflects variability along bathymetric contours that is greatest in the shallowest layers. This variability along bathymetric contours necessarily comes from processes other than the model derived above (Eq. 8). Because the GOM basin-mean trend is removed at each grid point prior to comparison with ζ_b^*, these trends necessarily reveal the redistribution of water from regions deeper than ~ 150 m, to those shallower. In the absence of additional forcings, the redistribution predicted by ζ_b^* (Eq. 8) should identically match ζ_b'. That they agree to the extent seen in Figure 6 suggests this sub-surface warming-driven redistribution is a dominant mechanism driving the spatial structure of coastal RSL rise at decadal timescales. The GOM hypsometric curve (Fig. 2b) and the depth and magnitude of sub-surface warming together dictate the depth at which the decadal trends change sign, ~ 150 m, which is the depth contour at which the local steric height change equals the GOM basin-mean ζ_ρ change. Mapped back onto the ECCO GOM grid, ζ_b^* trends explain over $\sim 70\%$ of ζ_b' trends on average locally (Fig. 7c). This fraction is highest in the eastern GOM and along the continental shelf, where at the coast, the GOM basin-mean $\overline{\zeta_b}$ trend (2.3 mm yr^{-1}) and redistribution driven ζ_b^* trend (6.2 mm yr^{-1}) combine to a value of ~ 9 mm yr^{-1} over the 2008-2017 decade.

Taking advantage of the full ECCO record, we next consider temporal variability in decadal trends of $\overline{\zeta_b}$ and ζ_b' to investigate how unique the 2008-2017 period was and to what extent ζ_b^* and subsurface warming can explain ζ_b' trends. Comparison of predicted and model trends over 16 decade-long periods, each beginning in January of years 1993 through 2008, reveals similar trend map patterns across a majority of decades considered (Fig. 8). With the exception of the decade beginning in January of 2002, positive values of $\overline{\zeta_b}$ reflect net import of mass into the GOM at rates similar to barystatic sea-level rise that explains some fraction of RSL at the coast. One explanation as to why the 2002-2011 $\overline{\zeta_b}$ trend is negative is that the end of this decade coincides with a period of persistent La Niña-like conditions that caused rates of global mean sea-level rise to briefly change sign (Boening et al., 2012). Subtracting the $\overline{\zeta_b}$ trend at all grid points reveals regional ζ_b' trend patterns similar to those from the 2008-2017 period (Fig. 9). In each decade, excluding the one beginning in 2002, ζ_b' trends are generally positive on the shelf and negative on the slope and in deeper regions. The standard deviation of these trends, indicative of internal mass redistribution within the GOM, varies in concert with

[1] $x(z_i,t) = a\sin\left(\frac{2\pi}{365}t + b\right) + c\sin\left(\frac{2\pi}{365/2}t + d\right) + et + f$, where a and c are seasonal cycle amplitudes, b and d seasonal cycle phases, e the linear trend, and f the constant/intercept. These parameters are fit at each depth z_i across all times t.

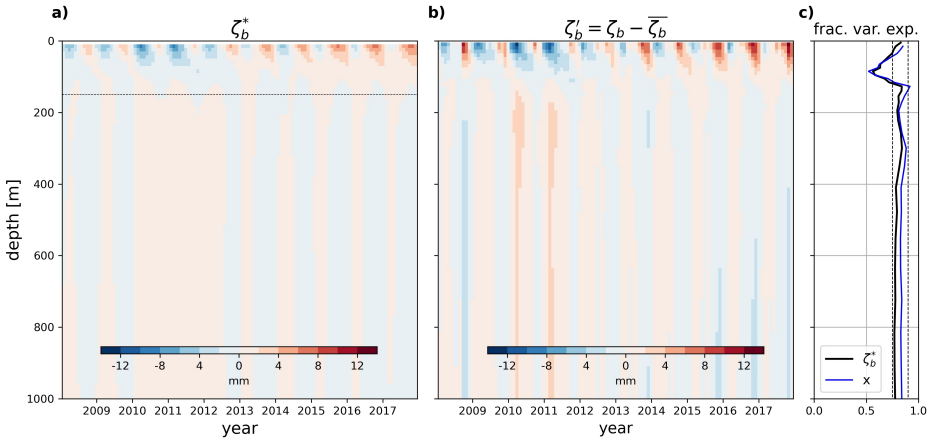

Figure 5. a) Hovmoller diagram of predicted changes in manometric sea-level ζ_b^* between the surface and 1000 m vs. time (2008-2017). Changes are shown relative to the ten year mean at each depth. The dashed black line is the approximate depth at which the ten year trend is zero. b) Hovmoller diagram of model manometric sea-level anomaly ζ_b' changes between 2008 and 2017. Values are averaged across all grid points within the depth bounds of each model layer. c) Fraction of ζ_b' variance explained by ζ_b^* at each depth (black). The blue profile is the fraction of variance explained by the seasonal cycle plus trend fit to ζ_b^*. Vertical dashed lines mark 0.75 and 0.9 values.

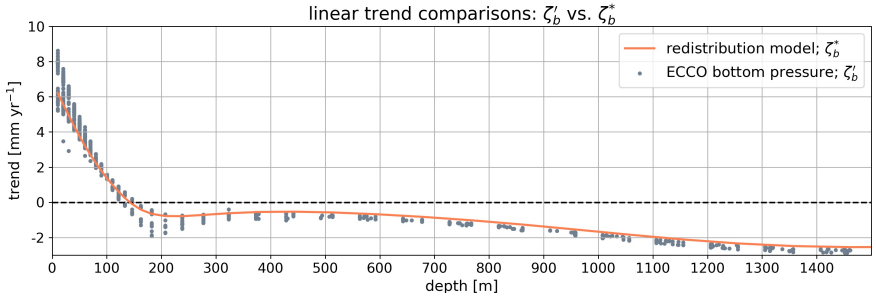

Figure 6. Mean ζ_b' trends averaged within depth bounds of each model (grey points). Predicted trend in bottom pressure ζ_b^* at each layer mid-point depth (orange). Trends are fit over the 2008-2017 period.

the $\overline{\zeta_b}$ time-series across the 16 decades, with 2008-2017 as the largest (Fig. 8). This suggests that the GOM tends to warm and gain mass simultaneously, and vice versa cool and lose mass in tandem. The standard deviations in ζ_b' trends increase after $\sim$ 2006 by nearly a factor of two from a mean spanning the 1993 - 2006 period. If redistribution due to warming at depths below the shelf break is the only contributor to trends in ζ_b', this suggests a significant increase in subsurface warming since 2006 and a potential source responsible for the GOM uniqueness identified in Sweet et al. (2022). Shoreward of the shelf break, ζ_b' trends between 2006 and 2017 exceed 5 mm yr^{-1}, a near five-fold increase compared those at the same locations between 1993 and 2006.

Over 16 decade-long periods, a tight correspondence is observed between upper ocean ζ_b' and ζ_b^* trends (Fig. 10). Despite variability in ζ_b' trends across the depths spanning each layer, mean trends are well predicted by ζ_b^*. In a few decadal periods, particularly

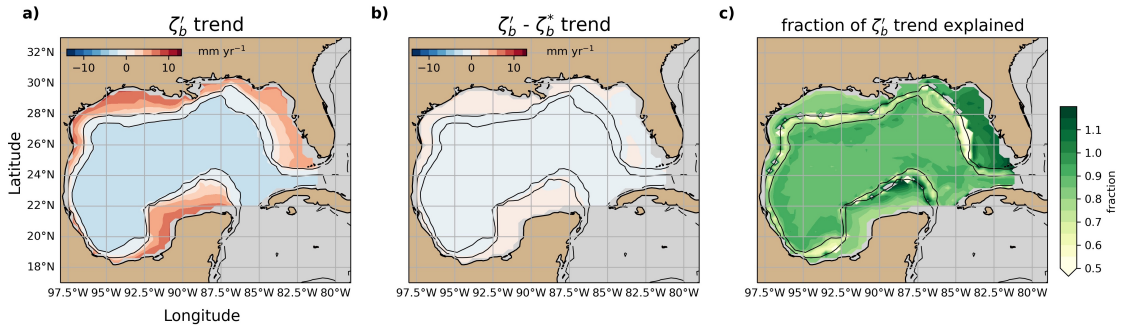

Figure 7. a) 2008-2017 model manometric sea-level anomaly trend ζ_b'. b) Difference between model (a) and predicted bottom pressure ζ_b^*. c) Fraction of ζ_b' trend explained by ζ_b^*

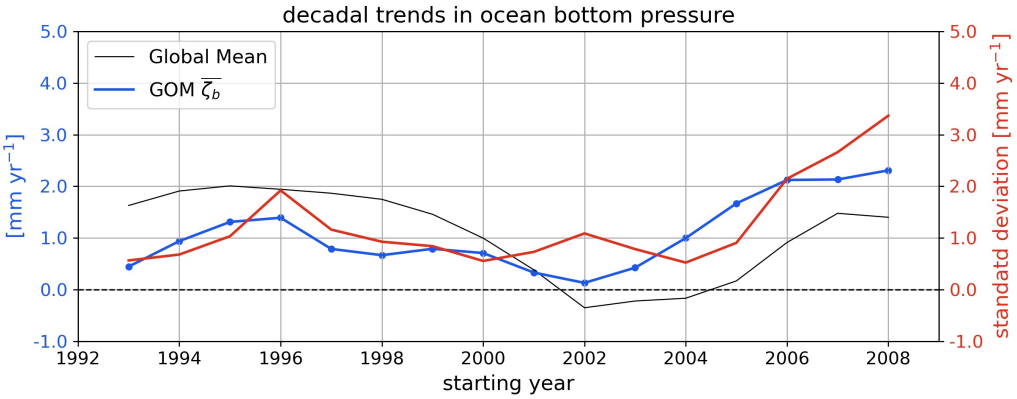

Figure 8. ECCO GOM mean manometric sea-level $\overline{\zeta_b}$ trend for 16 decade-long periods (blue). Horizontal axis identifies the starting year of each decade long period. The global mean is in black. Standard deviations of ζ_b', the bottom pressure trends after removal of the GOM mean trend, are in red.

those beginning in the early 2000's, both model and predicted trends are negative, implying a movement of water off of the continental shelf and suggestive of deeper cooling. The most recent decades, however, experience the greatest subsurface warming across the entire ECCO record (e.g., yellow dots in the top right quadrants of Fig 10a,b).

3 Observations

Results in Section 2 predict that a significant fraction of coastal RSL rise can be explained as the sum of subsurface warming driven redistribution and net import of mass into the GOM. In this section we test this model-based hypothesis using observations. All variables used in this section represent observation-based estimates unless otherwise stated.

3.1 Measurement Platforms

Altimeter-derived fields of ζ, gridded at 0.25-degree resolution across the 1993-2021 period, are produced by Ssalto/Duacs and provided by the EU Copernicus Marine Environmental Monitoring Service (Taburet et al., 2019). This product is the result of merged and optimally interpolated SSH measurements from multiple nadir-pointing satellite-altimeter

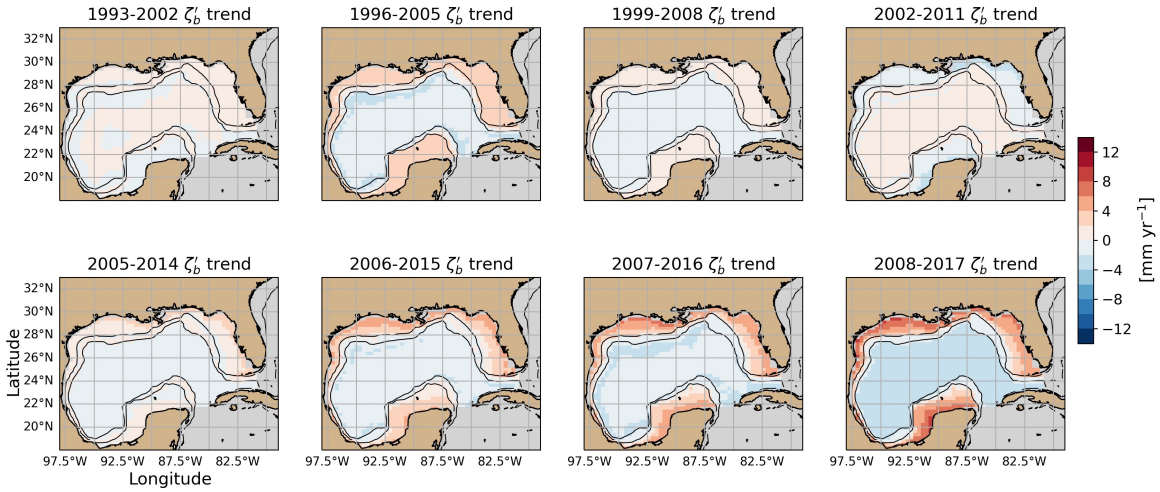

Figure 9. ECCO GOM manometric sea-level trends for 8 of the 16 decades. Decadal trends are shown at three-year intervals, switching to one year after that beginning in 2005. Subplot titles label the starting year of each decade. In each, the basin mean trend (Fig. 8) has been removed.

missions. These data, referenced to a 20-year mean SSH, are first smoothed with a 30-day boxcar filter before fitting linear trends. Coastal sea-level records at 19 tide gauge stations along the US GOM coast are downloaded from the Permanent Service for Mean Sea Level (Holgate et al., 2013). At many of these stations records begin in 1970, but all are complete over the 1993-present period. At these same locations, linear rates of VLM estimated using global positioning system (GPS) measurements referenced to the International Terrestrial Reference Frame are obtained from the the Nevada Geodetic Laboratory (Hammond et al., 2021). These rates are assumed to be near constant over the $\sim$ 30 year period of interest in this study. Rates are subsequently subtracted from linear RSL tide gauge trends to enable appropriate comparison to altimeter and ζ_b trends. Measurements of ζ_b derive from GRACE and GRACE Follow-On (FO) missions and extend from 2002 to present (Watkins et al., 2015; Wiese et al., 2016, 2018; Landerer et al., 2020). The horizontal resolution of these measurements is limited to 3° x 3° regions using the most recent Jet Propulsion Laboratory Mascon (GRCTellus RL06M.MSCNv02CRI). Thousands of temperature and salinity profiles, collected in the GOM by Argo profiling floats since 2010, are used to calculate in-situ density over the upper 1000 m (Fig. 11) (Argo, 2020). These profiles are restricted to regions where GOM depth exceeds 1000 m. While measurements were first made in 2010, profile coverage and density increases significantly after $\sim$ 2014.

3.2 Results

Basin -mean and -anomaly ($\overline{\zeta_b}$ and ζ_b') trends derived from GRACE/GRACE-FO measurements compare favorably to ECCO equivalents after re-gridding to the relevant Mascon (Fig. 12a,b). In addition to positive basin mean model- and observation- based trends ($\sim$ 3.7 mm yr^{-1} and $\sim$ 2.9 mm yr^{-1} respectively), both maps reveal positive ζ_b' trends along the Yucatan, eastern, and northern shelves, and negative trends in the interior GOM. This spatial pattern only changes slightly when shifting the decade over which trends are fit to align with the earliest decade of consistent Argo float profiling (Fig. 12c). Agreement of ζ_b' trends in spatial pattern and amplitude between model and observa-

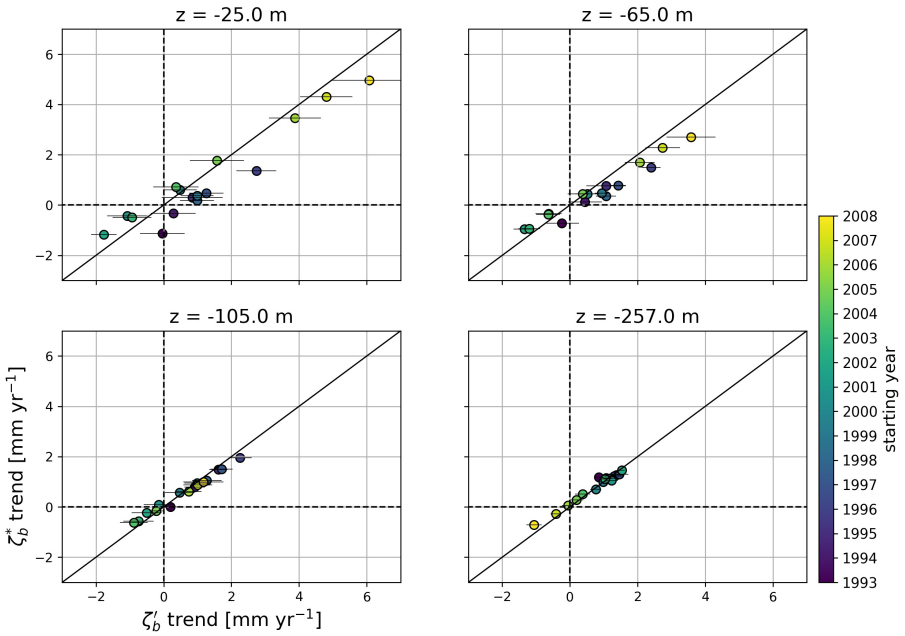

Figure 10. Model ζ_b vs predicted ζ_b^* trends at four depths. Color indicates the starting year of the decade long period over which trends are fit. Black line is a reference slope of one. Horizontal lines corresponding to each point are ± one standard deviation of ζ_b' trends within depth ranges spanned by each model layer.

tions further affirms ECCO as a valuable tool to investigate physical processes of relevance to coastal RSL rise. With this result, $\overline{\zeta_b}$ estimates from GRACE/GRACE-FO can next be used along with VLM estimates, to determine the ζ_b^* contribution from Argo data to coastal RSL trends at GOM tide gauge stations.

The earliest decade of overlap between GRACE/GRACE-FO and Argo measurements (2010-06 – 2020-06) is noteworthy as one in which altimeter derived rates of sea-level rise is elevated relative to longer-term behavior (e.g., Fig. 1e, trend line). To arrive at an estimate of the impact of warming on coastal RSL rise, predicted bottom pressure changes ζ_b^* are calculated from Argo densities profiles re-gridded to the ECCO vertical grid such that the same layer areas (A_i,A_s) defined in Section 2 can be used in Equation 8. Following the same procedure, densities are horizontally averaged within each layer. As in ECCO, these layer averages reveal subsurface warming at the decadal timescale, despite incomplete spatial coverage of profiles. These measurements are limited to the upper 1000 m and only in regions where the GOM depth is greater than 1000 m, but recalculation of ECCO results in Section 2 over these extents show essentially no change in the agreement between ζ_b and ζ_b^* trends (not shown). The linear trend in Argo-based estimates of ζ_b^* for 2010-2020 identify warming-driven mass distribution, where now we are interested in ζ_b^* at the coast.

When combined, an estimate of the rate of sea-level rise expected at the coast due to offshore subsurface warming, $\zeta_b^*(z = 0)$, and due to a net import of mass into the GOM, $\overline{\zeta_b}$, explains a large fraction of variability observed at the coast (Fig. 13, Table 1). This variability at the coast is again characterized as a linear trend fit over the 2010-

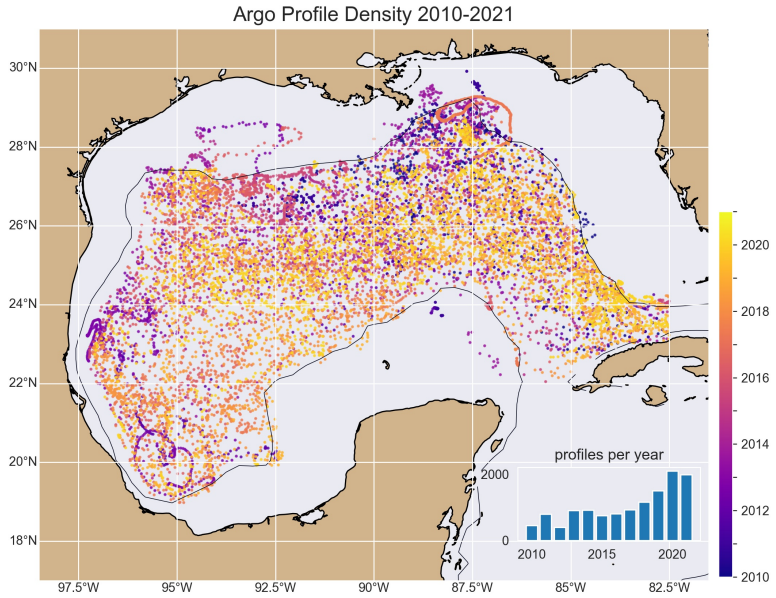

Figure 11. Locations of individual Argo profiles between 2010 and 2019. Profiles are colored by year with the 1000 m isobath in black. Inset shows total number of float profiles per year.

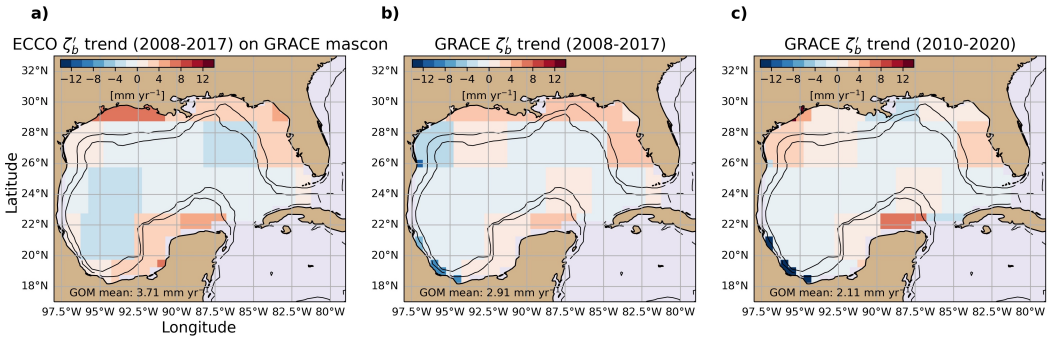

Figure 12. a) ECCO 2008-2017 bottom pressure trend on GRACE Mascon with GOM basin mean trend (at the bottom left) removed. b) GRACE equivalent for the 2008-2017 period. c) GRACE equivalent for the 2010-2019 period. GRACE GOM ocean mask is the same as that defined in Section 2.1. These trends are computed on timeseries in which the global mean is not removed.

2020 decade to tide gauge records that are each adjusted by a unique VLM estimate. That these trends are all positive, generally increasing in magnitude moving east to west, reveals a regional pattern, highlighting tide-gauge co-variability, of sea-level rise that is consistent with observed bottom pressure and warming trends. Comparison of the respective contributions from net mass import (2.1 mm yr^{-1}) and redistribution (4.7 mm yr^{-1}) processes reveal that subsurface warming is twice as important in driving sea-level rise at the coast. At each tide gauge station, the fraction of sea-level rise explained by these

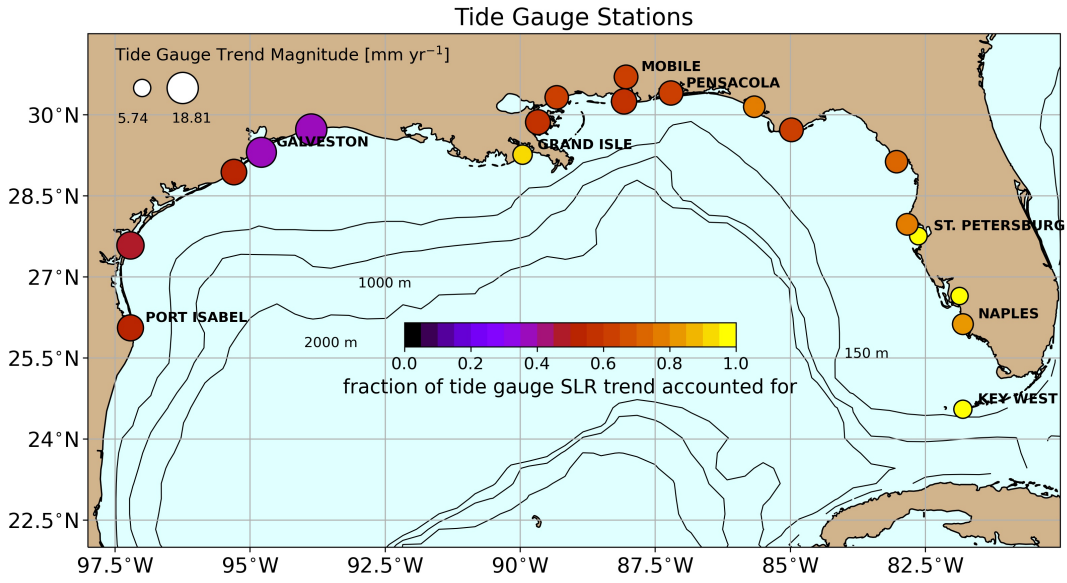

Figure 13. Locations of 19 tide gauge stations along the U.S. Gulf of Mexico coast (subset of 8 are labeled). Circle size corresponds to the magnitude of sea-level trend over the 2010-2019 period after removal of VLM estimates. Circle color identifies the trend fraction explained by both GRACE/GRACE-FO ($\overline{\zeta_b}$, reflective of mass transport into the Gulf) and Argo (ζ_b^* due to subsurface warming) measurements.

summed contributions increases moving west to east (Fig. 13), with values the eastern GOM exceeding 0.8. While the trend fraction accounted for is relatively high, these results do not suggest a lack of contribution from other processes (e.g., local atmospheric variability; Kolker et al. (2011)). These results suggest that along the Florida coast in particular, recent positive trends in RSL rise can be largely understood as the result of an influx of mass into the GOM and a subsurface warming-driven redistribution of mass onto the shelf, with the latter producing a substantially larger contribution.

4 Discussion and Conclusions

In this analysis we investigated elevated rates of sea-level rise observed throughout the GOM in altimeter and tide gauge records (Fig. 1). In particular, we considered the contribution to decadal trends in coastal RSL rise by subsurface warming and identified a relationship between changes in ocean bottom pressure and warming at depths deeper than the shelf break. This investigation first made use of the ECCO Version 5 LLC270 state estimate to relate predicted trends in manometric sea-level ζ_b^* to ECCO trends in manometric sea-level anomaly ζ_b'. Predicted trends derive from subsurface density changes, the result of ocean warming, occurring throughout the 25 years of model output (1993-2017). Trends in subsurface warming and bottom pressure were considered on decadal time-scales and focus drawn to the 2008-2017 decade as it corresponds to a period of elevated rates of sea-level rise in the GOM and broader North Atlantic (Figs. 1, 3a). On these timescales, we found the contribution of mass redistribution towards the coast caused by subsurface warming explains over 75% of the trends in ζ_b' (Figs. 5, 6, and 7). This fraction explained is greatest along the west Florida continental shelf. The magnitudes of the positive trends on the shelf are controlled by both the magnitude of subsurface warming, but also the ratio of the layer area in which warming occurs to

surface layer area. This distribution of areas and the profile of warming uniquely shapes a coastal response.

In addition to this response to warming, coastal RSL rise is driven by an overall increase in GOM mass (Fig. 3c), increasing at a rate similar to barystatic sea-level due to terrestrial water storage and land-ice melt. And while the 2008-2017 period was one of elevated sea-level rise throughout the GOM, decadal trends in $\overline{\zeta_b}$ over the full 1993 - 2017 ECCO run reveal a near continuous increase in GOM mass (Fig. 8). On top of this, mass redistribution indicated by trends in ζ_b' reveal an additional increase in shallow regions (Fig. 9). Considered in 16 decade-long periods, trends in ζ_b^* can almost entirely explain trends in ζ_b' (Fig. 10). This suggests that a subsurface warming driven response, largely revealed by patterns in ζ_b' trends, contributes importantly to RSL rise at the coast. These conclusions ignore any other static and dynamic effects on sea-level trends that may be due to local changes in atmospheric forcing or ocean dynamics within the GOM.

Using Argo float temperature and salinity measurements and GRACE/GRACE-FO derived bottom pressure measurements, decadal trends over the 2010-06 – 2020-06 period were next evaluated against coastal records of RSL rise. The fraction of these trends explained by net mass import into the GOM and warming-driven redistribution accounts for 33% to 90% of the trends observed (Fig. 13). In the eastern GOM in particular, these processes account for over $\sim 80\%$ of the those observed. Disagreement between predicted and observed trends, especially in the western GOM, may reflect VLM at space and time scales not captured by the GPS data (Kolker et al., 2011; Liu et al., 2020). Additional processes unaccounted for here include effects of regional variation in atmospheric forcing, basin circulation dynamics, and error in warming trends estimated from Argo profiles due to incomplete sampling of the basin.

The decadal sea-level variability evident within the GOM is not confined to the GOM. As revealed by Volkov et al. (2019), SSH in the GOM co-varies with that throughout the subtropical North Atlantic gyre (Volkov et al. (2019), Fig. 1a,e), especially on GOM continental shelves. Volkov et al. (2019) notably highlight that variability on the shelf is related to patterns of warming over the broader region, where offshore variability includes mesoscale eddy contributions at shorter time scales. They also consider effects of large scale heat divergence across the subtropical gyre on coastal sea-level, but do not elaborate on specific mechanisms mediating the relationship between open-ocean and coastal sea-level. In this study we specifically consider warming within the GOM and identify a mechanism by which more local subsurface warming in particular contributes significantly to coastal sea-level rise at decadal timescales. That GOM mean and subtropical gyre mean steric height trends over the 2010-2020 decade are similar in magnitude (~ 6.8 mm yr^{-1} and ~ 7.7 mm yr^{-1} respectively) affirms this connection to the North Atlantic and places GOM coastal sea-level rise in a broader context.

The coastal response to offshore subsurface warming explored here is shaped by the magnitude and depths of warming and the regional hypsometry. Only warming over a fraction of the total GOM surface area can drive a redistribution of mass towards the coast that is evident in bottom pressure trends. For simple bathymetric geometries, like the schematic in Figure 4, this implies that the minimum depth of warming coincident with a mass redistribution is equal to the bathymetric contour at which bottom pressure anomaly trends change sign. Throughout the decades considered here, that depth is not shallower than ~ 150 m. While this relationship is easily considered in the GOM because it is a nearly enclosed basin with ocean depths monotonically increasing offshore, the extent of its broader relevance motivates future work that can likewise make use of the satellite gravimetric record. These results reveal bottom pressure fields to include an imprint of subsurface warming contributing to sea-level rise at the coast and show that GRACE/GRACE-FO measurements can be effectively used to disentangle patterns of ocean warming.

Our results raise the question as to the source of the subsurface warming that drives internal mass redistribution contributing to coastal sea-level trends. One hypothesis is that the warming relates to variable heat transport by Loop Current eddies. A recent survey and characterization of Loop Current eddies by Meunier et al. (2020, 2022) details their role as vehicles for subsurface heat transport into the GOM. These eddies form following instability in the Loop Current and propagate into the interior with core depths greater than 150 m. In their analysis, authors conclude that these eddies represent a principle positive heat flux into the GOM, resulting in eddy decay and heat loss to the surrounding GOM waters. Because these eddies are generated at irregular intervals and their size can vary between $\sim$ 50 and $\sim$ 200 km, trends in heat content anomalies entering the GOM, however, remain difficult to diagnose. Despite this difficulty, Domingues et al. (2018) and Ibrahim and Sun (2020) show that 2010-2015 was a period of warming of waters that feed the Loop Current. These results suggest a link between the GOM and a broader region in which Loop Current eddies may propagate warming signals into the GOM that contribute to coastal sea-level via the mechanism presented here.

This analysis demonstrates the value of satellite observations of SSH and ocean bottom pressure in revealing how coastal sea-level changes relate to larger scale climate changes. Here, this connection is described using a mechanistic framework in which the vertical structure of ocean warming and regional hyspometry shape a coastal response. With density and bottom pressure measurements alone, these results suggest that a significant fraction of coastal sea-level rise can be anticipated or inferred. Questions of how well this prediction works and its dependence on regional hypsometry motivate similar analyses in other regions to investigate local and remote drivers of coastal sea-level rise. That predicted decadal trend patterns in bottom pressure agree with those observed futher motivates the continued collection of these measurements such that regional variability can be rigorously investigated on decadal and longer timescales.

Table 1. Decadal Trends (ECCO; 2008 – 2017, all others; 2010-06 – 2020-06) and trend Standard Error. Standard Error is determined using Fourier phase scrambling (Piecuch et al., 2017) (procedure: Fast Fourier Transform is taken of each time series, phases are randomly scrambled 1000 times, inverse transform taken, and a linear trend is fit to each series). The Standard Error is taken as the standard deviation of this distribution of trends (Bos et al., 2013; Theiler et al., 1992). Comparison to observed trends show them to all be significant.

Source	Trend [mm yr^{-1}]	Std. Error [mm yr^{-1}]
ECCO GOM bottom pressure $\overline{\zeta_b}$	2.3	$\pm$ 1.3
ECCO Eq. 8 prediction ζ_b^* at z = -5 m	6.2	$\pm$ 3.3
Tide Gauge SSH[a]		
Key West, FL	7.8	$\pm$ 4.1
Naples, FL	9.9	$\pm$ 4.2
St. Petersburg, FL	7.5	$\pm$ 3.7
Pensacola, FL	13.6	$\pm$ 7.1
Mobile, AL	12.9	$\pm$ 5.8
Grand Isle, LA	14.2	$\pm$ 7.2
Galveston, TX	20.6	$\pm$ 11.7
Port Isabel, TX	14.8	$\pm$ 8.3
GRACE GOM bottom pressure $\overline{\zeta_b}$	2.1	$\pm$ 1.4
Argo Eq. 8 prediction ζ_b^* at z = -5 m	4.7	$\pm$ 3.3

[a] estimated VLM contribution is removed

Open Research Section

Gridded sea level anomalies produced by Ssalto/Duacs were obtained from the Copernicus Marine Environmental Monitoring Service (https://doi.org/10.48670/moi-00148) (https://resources.marine.copernicus.eu/product-detail/SEALEVEL_GLO_PHY_L4_MY_008_047). Tide gauge measurements were downloaded from the Permanent Service for Mean Sea Level (https://www.psmsl.org/data/). Corresponding rates of vertical land motion at tide gauge stations were downloaded from (http://geodesy.unr.edu/vlm.php). Argo profiles were obtained using Argopy (https://argopy.readthedocs.io/en/latest/index.html). These data were collected and made freely available by the International Argo Program and the national programs that contribute to it (https://argo.ucsd.edu, https://www.ocean-ops.org). The Argo Program is part of the Global Ocean Observing System. Bottom pressure measurements at ~ 3 degree resolution (JPLTellus mascon) derived from GRACE/GRACE-FO measurements were downloaded from (http://grace.jpl.nasa.gov). Python scripts developed and used in this analysis are available on GitHub (https://github.com/jakesteinberg/nasa_ostst).

Acknowledgments

J. Steinberg was supported by N.A.S.A. Jet Propulsion Laboratory Subcontract 1670515, C. Piecuch supported by N.A.S.A. grants 80NSSC20K0728 & 80NSSC20K1241, and B. Hamlington's contribution carried out at the Jet Propulsion Laboratory, California Institute of Technology, under a contract with the National Aeronautics and Space Administration. P. Thompson and S. Coats were supported by N.A.S.A. under the Ocean Surface Topography from Science Team. We would like to thank the ECCO project and community for help in obtaining and analyzing model output.

References

Argo. (2020). Argo float data and metadata from global data assembly centre (argo gdac). *SEANOE*. doi: https://doi.org/10.17882/42182

Bingham, R., & Hughes, C. (2012). Local diagnostics to estimate density induced sea-level variations over topography and along coastlines. *Journal of Geophysical Research*, *117*. doi: 10.1029/2011JC007276

Boening, C., Willis, J., Landerer, F. W., Nerem, R., & Fasullo, J. (2012). The 2001 la niña: So strong, the oceans fell. *Geophysical Research Letters*, *39*. doi: https://doi.org/10.1029/2012GL053055

Bos, M., Williams, S., Araujo, I., & Bastos, L. (2013). The effect of temporal correlated noise on the sea level rate and acceleration uncertainty. *Geophysical Journal International*, *196*. doi: 10.1093/gji/ggt481

Buckley, M., & Marshall, J. (2016). Observations, inferences, and mechanisms of the atlantic meridional overturning circulation: A review. *Reviews of Geophysics*, *54*. doi: https://doi.org/10.1002/2015RG000493

Domingues, R., Goni, G., Baringer, M., & Volkov, D. (2018). What caused the accelerated sea level changes along the u.s. east coast during 2010-2015. *Geophysical Research Letters*, *45*. doi: https://doi.org/10.1029/2018GL081183

Forget, G., Campin, J., Heimbach, P., Hill, C., Ponte, R., & Wunsch, C. (2015). Ecco version 4: an integrated framework for non-linear inverse modeling and global ocean state estimation. *Geoscientific Model Development*, *8*. doi: 10.5194/gmd-8-3071-2015

Fukumori, I., Heimbach, P., Ponte, R., & Wunsch, C. (2018). A dynamically consistent, multivariable ocean climatology. *Bulletin of the American Meteorological Society*, *99*. doi: https://doi.org/10.1175/BAMS-D-17-0213.1

Gill, A., & Niler, P. (1973). The theory of the seasonal variability in the ocean. *Deep-Sea Research*, *20*, 141-177. doi: https://doi.org/10.1016/0011-7471(73)90049-1

Greatbatch, R. (1994). A note on the representation of steric sea level in models

that conserve volume rather than mass. *Journal of Geophysical Research*, *99*. doi: 10.1029/94JC00847

Gregory, J., Griffies, S., Hughes, C., Lowe, J., Church, J., Fukumori, I., ... van de Wal, R. (2019). Concepts and terminology for sea level: Mean, variability and change, both local and global. *Surveys in Geophysics*, *40*. doi: https://doi.org/10.1007/s10712-019-09525-z

Hamlington, B., Chambers, D., Frederikse, T., Dangendorf, S., Fournier, S., Buzzanga, B., & Nerem, S. (2022). Observations-based trajectory of future sea level for the coastal united states tracks near high-end model projections. *Communications Earth and Environment*, *3*. doi: https://doi.org/10.1038/s43247-022-00537-z

Hammond, W., Blewitt, G., Kreemer, C., & Nerem, R. (2021). Gps imaging of global vertical land motion for studies of sea level rise. *Journal of Geophysical Research: Solid Earth*, *126*. doi: https://doi.org/10.1029/2021JB022355

Holgate, S., Matthews, A., Woodworth, P., Rickards, L., Tamisiea, M., Bradshaw, E., ... Pugh, J. (2013). New data systems and products at the permanent service for mean sea level. *Journal of Coastal Research*, *29*. doi: https://doi.org/10.2112/JCOASTRES-D-12-00175.1

Ibrahim, H. D., & Sun, Y. (2020). Mechanism study of the 2010-2016 rapid rise of the carribean sea level. *Global and Planetary Change*, *191*. doi: https://doi.org/10.1016/j.gloplacha.2020.103219

Jackett, D., & McDougall, T. (1995). Minimal adjustment of hydrographic profiles to achieve static stability. *Journal of Atmospheric and Oceanic Technology*, *12*. doi: 10.1175/1520-0426(1995)012⟨0381:MAOHPT⟩2.0.CO;2

Kolker, A., Allison, M., & Hameed, S. (2011). An evaluation of subsidence rates and sea-level variability in the northern gulf of mexico. *Geophysical Research Letters*, *38*. doi: 10.1029/2011GL049458

Landerer, F., Fletchtner, F., Save, H., Webb, F., Bandikova, T., Bertiger, W., ... Yuan, D.-N. (2020). Improved methods for observing earth's time variable mass distribution with grace using spherical cap mascons. *Geophysical Research Letters*, *147*. doi: https://doi.org/10.1029/2020GL088306

Landerer, F., Jungclaus, J., & Marotzke, J. (2007). Ocean bottom pressure changes lead to a decreasing length-of-day in a warming climate. *Geophysical Research Letters*, *34*. doi: 10.1029/2006GL029106

Liu, Y., Fasullo, J., & Galloway, D. (2020). Land subsidence contributions to relative sea level rise at tide gauge galveston pier 21, texas. *Scientific Reports*, *10*. doi: https://doi.org/10.1038/s41598-020-74696-4

Meunier, T., Perez-Brunius, P., & Bower, A. (2022). Recontructing the three-dimensional structure of loop current rings from satellite altimetry and in situ data using the gravest empirical modes method. *Remote Sensing*, *14*. doi: 10.3390/rs14174174

Meunier, T., Sheinbaum, J., Pallas-Sanz, E., Tenreiro, M., Ochoa, J., Ruiz-Angulo, A., ... de Marez, C. (2020). Heat content anomaly and decay of warm-core rings: the case of the gulf of mexico. *Geophysical Research Letters*. doi: 10.1029/2019GL085600

Piecuch, C., Ponte, R., Little, C., Buckley, M., & Fukumori, I. (2017). Mechanisms underlying recent decadal changes in subpolar north atlantic heat content. *JGR: Oceans*, *122*. doi: https://doi.org/10.1002/2017JC012845

Piecuch, C., Thompson, P., Ponte, R., Merrifield, M., & Hamlington, B. (2019). What caused recent shifts in tropical pacific decadal sea-level trends? *JGR: Oceans*, *124*. doi: https://doi.org/10.1029/2019JC015339

Ponte, R. (2006). Oceanic response to surface loading effects neglected in volume-conserving models. *Journal of Physical Oceanography*, *36*. doi: 10.1175/JPO2843.1

Sweet, W., Hamlington, B., Kopp, R., Weaver, C., Barnard, P., Bekaert, D., ...

Zuzak, C. (2022). Global and regional sea level rise scenarios for the united states: Up-dated mean projections and extreme water level probabilities along u.s. coastlines. *NOAA Technical Report NOS 01, National Oceanic and Atmospheric Administration, National Ocean Service, Silver Spring, MD*.

Sweet, W., Kopp, R., Weaver, C., Obeysekera, J., Horton, R., Thieler, E., & Zervas, C. (2017). Global and regional sea level rise scenarios for the united states. *NOAA Technical Report NOS CO-OPS 083, National Oceanic and Atmospheric Administration, National Ocean Service, Silver Spring, MD*.

Taburet, G., Sanchez-Roman, A., Ballarotta, M., Pujol, M.-I., Legeais, J.-F., Fournier, F., ... Dibarboure, G. (2019). Duacs dt2018: 25 years of reprocessed sea level altimetry products. *Ocean Sci.*, *15*. doi: https://doi.org/10.5194/os-15-1207-2019

Theiler, J., Eubank, S., Longtin, A., Galdrikian, B., & Farmer, J. (1992). Testing for nonlinearity in time series: the method of surrogate data. *Physica D: Nonlinear Phenomena*, *58*. doi: https://doi.org/10.1016/0167-2789(92)90102-S

Thompson, P., & Mitchum, G. (2014). Coherent sea level variability on the north atlantic western boundary. *JGR: Oceans*, *119*. doi: https://doi.org/10.1002/2014JC009999

Thompson, P., Piecuch, C., Merrifield, M., McCreary, J., & Firing, E. (2016). Forcing of recent decadal variability in the equatorial and north indian ocean. *JGR: Oceans*, *121*. doi: https://doi.org/10.1002/2016JC012132

Vinogradova, N., Ponte, R., & Stammer, D. (2007). Relation between sea level and bottom pressure and the vertical dependence of oceanic variability. *Geophysical Research Letters*, *34*. doi: 10.1029/2006GL028588

Volkov, D., Lee, S., Domingues, R., Zhang, H., & Goes, M. (2019). Interannual sea level variability along the southeastern seaboard of the united states in relation to the gyre-scale heat divergence in the north atlantic. *Geophysical Research Letters*, *46*. doi: 10.1029/2019GL083596

Watkins, M., Wiese, D., Yuan, D.-N., Boening, C., & Landerer, F. (2015). Improved methods for observing earth's time variable mass distribution with grace using spherical cap mascons. *Journal of Geophysical Research: Solid Earth*, *120*. doi: https://doi.org/10.1002/2014JB011547

Wiese, D., Landerer, F. W., & Watkins, M. (2016). Quantifying and reducing leakage errors in the jpl rl05m grace mascon solution. *Water Resour. Res.*, *52*, 7490-7502. doi: 10.1002/2016WR019344

Wiese, D., Yuan, D.-N., Boening, C., Landerer, F. W., & Watkins, M. (2018). Jpl grace mascon ocean, ice, and hydrology equivalent water height release 06 coastal resolution improvement (cri) filtered version 1.0 ver. 1.0. *PO.DAAC, CA, USA.*. doi: http://dx.doi.org/10.5067/TEMSC-3MJC6

Woodworth, P., Melet, A., Marcos, M., Ray, R., Wöppelmann, G., Sasaki, Y., ... Merrifield, M. (2019). Forcing factors affecting seat level changes at the coast. *Surveys in Geophysics*, *40*. doi: https://doi.org/10.1007/s10712-019-09531-1

Wunsch, C., & Heimbach, P. (2007). Practical global oceanic state estimation. *Physica D*, *230*. doi: https://doi.org/10.1016/j.physd.2006.09.040

Wunsch, C., Heimbach, P., Ponte, R., Fukomori, I., & ECCO-GODAE-Consortium. (2009). The global general circulation of the ocean estimated by the ecco-consortium. *Oceanography*, *22*. (http://www.jstor.org/stable/24860962)